Understanding the resolution and sensitivity in photothermal nanoscale chemical imaging - a point spread function approach

Yide Zhang,[†,‡] Ufuk Yilmaz,[†] Liam O'Faolain,[‡] Bernhard Lendl,[†] and Georg Ramer[*,†]

†*Institute of Chemical Technologies and Analytics, TU Wien, Vienna, 1060,Austria*

‡*Centre for Advanced Photonics and Process Analysis, Munster Technological University, Cork, T12P928, Ireland*

E-mail: georg.ramer@tuwien.ac.at

Abstract

Atomic force microscopy-infrared spectroscopy (AFM-IR) is a photothermal scanning probe technique that combines nanoscale spatial resolution with the chemical analysis capability of mid-infrared spectroscopy. Using this hybrid technique, chemical identification down to the single molecule level has been demonstrated. However, the mechanism at the heart of AFM-IR, the transduction of local photothermal heating to cantilever deflection, is still not fully understood. Existing physical models only describe this process in few special cases but not in many of the types of sample geometries encountered in the practical use of AFM-IR.

Here, we introduce an analytical expression for modeling the temperature and photothermal expansion process, verified with finite element simulations and validated with AFM-IR experiments. This method describes AFM-IR signal amplitudes in vertically and laterally heterogeneous samples and allows us to study the effect of the position

and size of the absorber as well as laser repetition rate and pulse width on AFM-IR signal amplitudes and spatial resolution.

Theses results will help experimentalists to select optimal AFM-IR settings and to achieve high signal intensity and resolution in AFM-IR experiments. The results also point towards the importance of interfacial thermal resistance and its contribution to AFM-IR imaging contrast. Understanding the significance and role of this so far hardly considered parameter will help to better understand the working principles of advanced AFM-IR modes such as tapping AFM-IR or surface sensitive AFM-IR.

Introduction

AFM-IR is a near-field technique combining atomic force microscopy (AFM) and mid-infrared (IR) spectroscopy, which achieves nanoscale spatial resolution optical imaging independent of the wavelength [1–3] and thus enables chemical analysis based on infrared spectroscopy orders if magnitude below the diffraction limit [4–8].

A typical AFM-IR setup consists of a pulsed laser focused onto a sample at the location of the tip of an AFM cantilever (see Fig. 1a). In general, the working principle of this technique [2,9] is described by focusing on the change of the sample's density, which induces a localized sample expansion. The partial or total absorption of light from the pulsed laser by molecules distributed in the sample results in a local temperature increase affecting the density and refractive index of the sample at the place of absorption. A train of laser pulses will thus generate a modulated temperature change in the sample leading to photothermal and photoacoustic waves that propagate within the sample. AFM-IR employs the the spatially resolved detection of the photothermal expansion of the sample by the AFM's cantilever upon illumination with a pulsed light source (see Fig. 1b). Absorption of light from the laser pulse leads to local temperature increase and concurrent thermal expansion (Fig. 1c). As the heat is redistributed within the sample this local expansion subsides.

Using a laser with adjustable pulse repetition rate, the mechanical resonances of

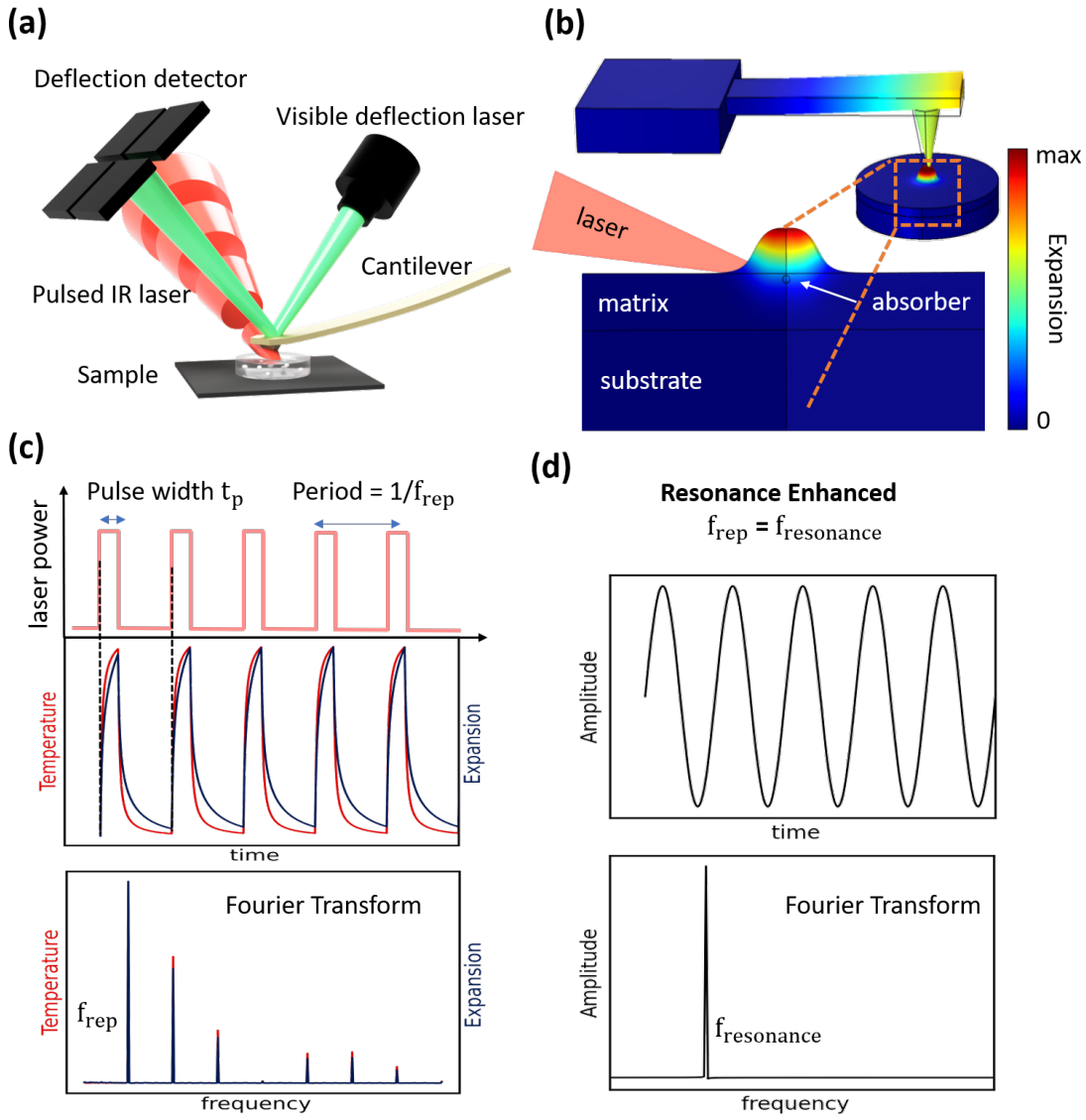

Figure 1: **Schematic illustration of the resonance enhanced AFM-IR.** **(a)** Sketch illustrating the AFM-IR setup. The sample (gray) is placed on a piece of silicon and illuminated from top with a pulsed, tunable, infrared beam (red). **(b)** The sample location that absorbs the energy of IR laser which is then transformed into temperature change and thermal expansion. The sample's photothermal expansion excites the cantilever into oscillations. **(c)** In the excitation process, temperature and expansion increase during the pulse time (t_p) and repeat the same process with the repetition frequency (f_{rep}). The signal in frequency domain will only present at the f_{rep} and it's higher order modes . While operating AFM-IR at contact mode, in the resonance-enhanced operation **(d)**, f_{rep} matches the selected resonance frequency of the cantilever to resonantly exciting it, thereafter, the enhanced AFM-IR signal is proportional to the mode's quality factor.

the cantilever can selectively be excited[10] when the laser repetition rate matches the selected mode of the cantilever. In this scenario, the photothermal expansion stimulates the AFM cantilever at it's oscillations resonance frequency (Fig. 1d), hereby selectively amplifying the AFM-IR signal which can be demodulated from the AFM deflection signal.

This general working principle is well accepted in the community and the ability of AFM-IR for chemical imaging is well established, with applications ranging from materials[11,12] to biological samples[6,13,14] and photonics, perovskites[15], and semiconductors[2,16]. Several groups have studied the AFM-IR imaging contrast mechanism. The initial theoretical description of AFM-IR signal generation and transduction was established by Dazzi et al.[17,18], who considered a homogeneous sample without accounting for geometry, illuminated with single pulse laser. While this model does not describe the spatial resolution of AFM-IR, it shows that the thermal expansion is linearly proportional to the local absorption.

Later, Morozovska et al., studied the contrast formation mechanism of T-shape boundary between two materials in nanoscale IR spectroscopy[19]. In this model, using two semi-infinite materials with an interface orthogonal to the AFM scanning plane temperature distribution and mechanical displacement of both absorber and the neighboring material is descrcibed, taking into account various factors, including different IR-radiation absorption coefficients, thermo-physical and elastic properties of the two materials. These properties encompass thermal diffusivities, thermal conductivities, and elastic stiffness, as well as thermal expansion coefficients. This model indicates higher modulation frequency would provide a significantly higher spatial resolution. Schwartz et al.[20] devised an analytical model to depict the photothermal expansion of a homogenous sample, factoring in a single laser pulse. They considered the laser heating profile and performed numerical simulations on heterogeneous samples comprising two adjacent materials. This study aimed to elucidate the dependence of signal transduction efficiency and spatial resolution on laser pulse width, pulse shape, sample thermalization time and interfacial thermal resistance, etc. and found this model in

good agreement with their previous experimental investigations.[21,22]

However, in many cases AFM-IR samples do not conform to the geometries described in literature. Particularly, many samples consist of absorbers embedded within a larger matrix, such as inclusion bodies inside a cell[23], metal soaps in paint layers[24] or even organelles[25].

In the present work, we develop a model describing the whole AFM-IR signal generation process, starting with light absorption by an absorber embedded in a matrix until detection of the sample's surface expansion. This model takes into account thermal and mechanical properties of materials, as well as the size and position of the absorber. The vertically and laterally inhomogeneous sample comprising an analyt embedded in a matrix is relevant to a wide range of common AFM-IR applications such as the detection of organelles within a cell[26] or contamination within a polymer layer[27].

Our approach uses an analytical description of the time dependent heating and sample deformation based on Green's functions. This model is a better match to real-world problems encountered in the life and material sciences than previously described analytical models, such as lumped linear proportional models. It provides exact mathematical expressions for the variables of interest, yielding clear insights into their relationships in an easily interpretable form. While models based on finite element modeling (FEM) are able to incorporate more details, here, our approach excels in computational efficiency.

This Green's function approach, whereby the response of a system to an excitation is determined by convolving the distribution of the absorbers and the time domain shape of the pump laser pulse with a system response function has some interesting parallels to signal processing and optical microscopy: along the temporal axis, the sample can be understood to act as a low pass filter upon the excitation pulse shape and in the spatial dimension, our model exhibits similarities to a point spread function (PSF) that is typically used to understand and characterize spatial resolution in optical imaging. Thus, this "PSF model of AFM-IR" enables us to directly compare the spatial resolution in optical imaging techniques and with those achieved in AFM-IR.

Furthermore, it allows the efficient modeling of the response of samples with arbitrary absorber distribution.

To arrive at a PSF model of AFM-IR that can be algebraically handled, certain assumptions regarding the sample geometry and properties need to be made. To ensure the validity of these assumptions, we compare the PSF model to finite element simulations which we can validate against experimental AFM-IR data. Through this validation process, we observe a strong agreement between the PSF model of AFM-IR, finite element simulations, and experimental results.

With the validated PSF model of AFM-IR, we are able to make general predictions regarding the spatial resolution and signal intensity in AFM-IR. Specifically, we can investigate how these parameters are influenced by factors such as the pulse width and repetition rate of the excitation laser, as well as the thermal and mechanical properties of the sample. By leveraging the PSF model, we gain valuable insights into the fundamental aspects of AFM-IR and its performance characteristics.

We show that this model will help to understand how experimental parameters (pulse rate, pulse width, sample stiffness, sample geometry,...) influence the performance of advanced AFM-IR techniques, such as tapping mode AFM-IR[28], or the recently introduced surface sensitive AFM-IR[29].

Results and discussion

Modeling the AFM-IR signal

In laterally homogeneous samples, the surface expansion is proportional to the temperature change of the sample after a laser pulse, hence for such samples the signal can fairly accurately be described if only sample heating and thermal conduction are taken into account.[7] However, to study spatial resolution in AFM-IR, models that describe laterally heterogeneous samples are required. Here, surface displacement also depends on the elastic response of the sample,[19] as the inhomogeneous, absorber distribution de-

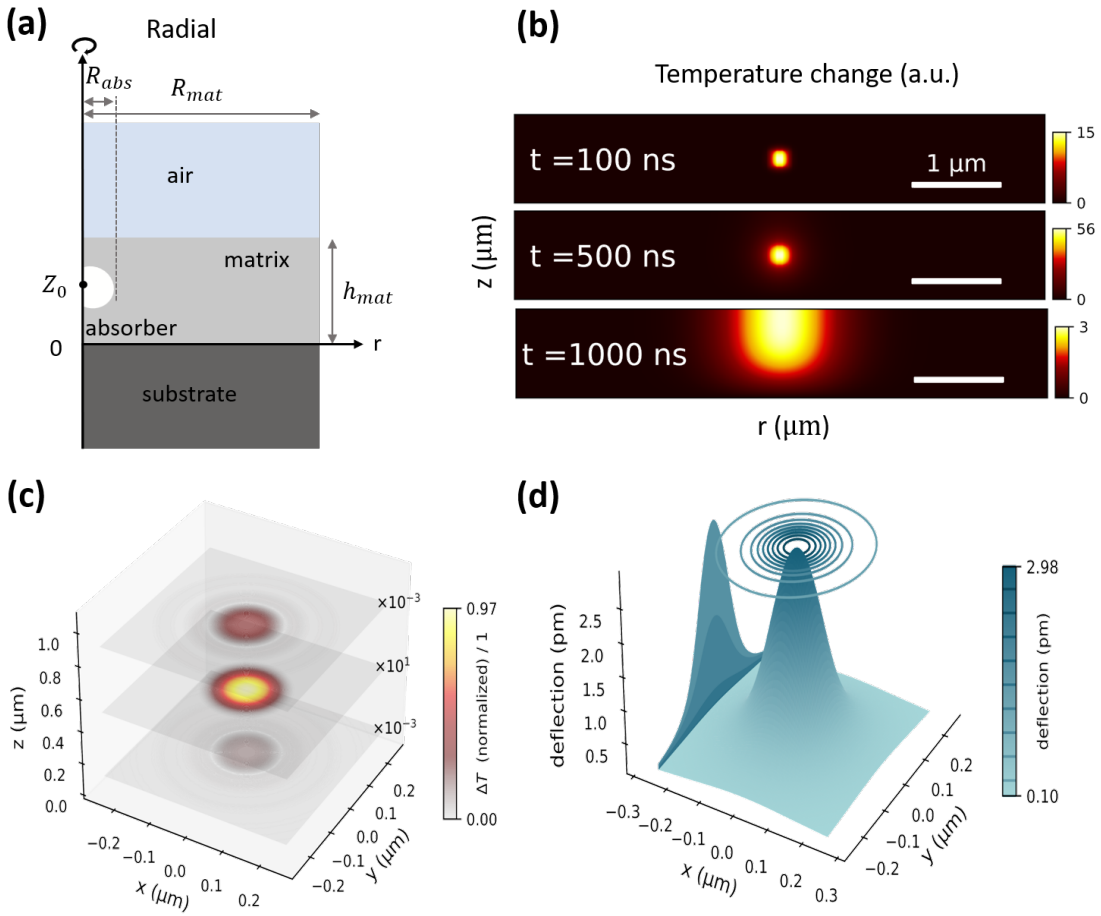

Figure 2: **Using the PSF model to describe the AFM-IR signal:** **(a)** Schematic of the modeled, cylindrically symmetric system composed of a single spherical absorber surrounded by a matrix, deposited on a non-absorbing substrate. **(b)** Lateral and vertical temperature change at different times during and after illumination with 500 ns length laser pulse. (Absorber position at $z_0 = 0.5\,\mu\text{m}$). **(c)** Amplitude of temperature change at several depths in the sample. **(d)** Amplitude of thermo-elastic displacement at the surface. At 500 kHz and a pulse width of 500 ns.

pendent heating and creates inhomogeneous strain in the neighboring material. There are three components in our description of AFM-IR: transient laser heating of the sample, heat conduction within the sample and thermo-elastic deformation of the sample.

More specifically, laser heating is described as a time dependent volumetric heat source $g(\mathbf{x}, t)$, where $\mathbf{x}$ represents any location in the domain. Thermal conduction is

described by Fourier's law

$$\bigtriangledown^2 T(\mathbf{x},t) + \frac{1}{\kappa} g(\mathbf{x},t) = \frac{1}{\alpha}\frac{\partial T(\mathbf{x},t)}{\partial t} \tag{1}$$

where κ is the thermal conductivity and α is the thermal diffusivity. In the equilibrium state, thermo-elastic sample deformation without external force is described by Navier's equations of thermoelasticity[30],

$$\mu \bigtriangledown^2 u_{\mathbf{x}} + (\lambda + \mu)\frac{\partial e}{\partial \mathbf{x}} - \beta \frac{\partial T(\mathbf{x},t)}{\partial \mathbf{x}} = 0 \tag{2}$$

where e is dilatation, λ and μ are the Lame elastic constants, and β is the thermo-elastic constant. The AFM-IR signal is proportional to the surface displacement. Depending on the type of transducer either the amplitude of displacement at a specific frequency[4] or the time dependent surface displacement[10] is recorded in AFM-IR. Considering the insignificance of the photoacoustic signal in AFM-IR measurements compared to the photothermal signal, along with its tendency to introduce artifacts[29], we have made the decision not to include it in the current model.

Assuming the system is in thermal equilibrium before excitation with a laser pulse, its response is determined through convolution of $g(\mathbf{x}',t)$ with a Green's function $G(\mathbf{x},t|\mathbf{x}',t')$. Green's function represents the temperature at any location $\mathbf{x}$ within the domain, at any time t, due to an instantaneous volumetric source, located at the position $\mathbf{x}'$, releasing its energy spontaneously at time $t = t'$ into a medium at steady-state conditions. To find G and solve Eq.(1) and (2), we use assumptions that have been previously shown to describe the thermal behavior of AFM-IR experiments well[7]: (1) the sample is a homogeneous material of known thickness that is (2) placed on a substrate acting as a heat sink and (3) covered by an insulating layer (air) (see Fig. 2a).

In the following sections we will first develop the analytical model, then verify that our model does not give significantly different results from a model that uses finite thermal conductivities for the cover layer and the substrate, by comparing the

results from the analytical model with those calculated using a finite element model (FEM). Model results are additionally compared to experimental AFM-IR data of a polymethyl methacrylate (PMMA) absober embedded in a polyethylene (PE) matrix. In the discussion section, we intend to present predictions regarding the resolution and signal intensity dependencies on the depth positions of the absorber, its size and the repetition rates of the laser.

The FEM simulations take into account additional factors, heat transfer between different materials, temperature distribution, thermal expansion in equilibrium states, and interfacial thermal conductance in agreement with other work[9,20,31]. For AFM-IR experiments, we prepared samples with PMMA beads embedded in PE matrix, and performed a series measurements with different laser pulse widths and repetition rates.

A Green's function solution describing the AFM-IR signal

We choose a cylindrical coordinate system, for two reasons: in analogy to PSFs, it allows an axi-symmetric, quasi-2D representation that is more illustrative than a three-dimensional one, without loss of generality, and has significantly lower computational cost for FEM modeling, required for comparison.

The heat equation in cylindrical coordinates reads

$$\frac{\partial^2 T(r,z,t)}{\partial r^2} + \frac{1}{r}\frac{\partial T(r,z,t)}{\partial r} + \frac{\partial^2 T(r,z,t)}{\partial z^2} + \frac{g(r,z,t)}{\kappa} = \frac{1}{\alpha}\frac{\partial T(r,z,t)}{\partial t} \tag{3}$$

using a finite, axisymmetric cylindrical sample of radius R_{mat} and height h_{mat}. Using the boundary conditions as outlined in the previous section the canonical Green's function solution[32] is

$$T(r,z,t) = \frac{\alpha}{\kappa}\int_{t'=0}^{t}\int_{z'=0}^{h_{mat}}\int_{r'=0}^{R_{mat}} G(r,z,t|r',z',t')g(r',z',t')r'dr'dz'dt' \tag{4}$$

with a Green's function

$$G(r,z,t|r',z',t') = \sum_{n=0}^{\infty}\sum_{m=0}^{\infty} \frac{4J_0(\beta_m r)sin(\eta_n z)}{h_{mat}R_{mat}^2 J_1^2(\beta_m R_{mat})} J_0(\beta_m r')sin(\eta_n z')e^{-\alpha\lambda_{nm}^2(t-t')} \quad (5)$$

where β_m, η_n and λ_{mn} are eigenvalues obtained according to boundary conditions (see Supplementary section S1). While G contains an infinite sum of modes, the decay time of each mode is $1/\alpha\lambda_{mn}^2$, which decreases as integer values m and n increase. Hence, the sum can be truncated once sufficiently short time scales have been reached.

The overall sample deformation in AFM-IR is on the order of picometers[7] and experimental parameters are chosen to not change sample properties (e.g. not to cause phase transitions or damage to the sample) during the experiment. Hence, we can split the time dependent, volumetric heat source in to a spatial and a temporal component $g(\mathbf{x},t) = g_V(\mathbf{x})g_t(t)$. The time domain variation in the illumination intensity is described by $g_t(t)$, while $g_V(\mathbf{x})$ describes the location and intensity of heating, i.e., location and magnitude of light absorption inside the sample (in the following discussion, we neglect optical effects such as interference upon the signal. These effects can be added by multiplying the absorption coefficient with the local light intensity to arrive at a modified g_V[32]). Splitting $g(\mathbf{x},t)$ allows us to also split the convolution in equation (5) into two parts, one that describes the mode amplitude and shape in r and z, and one that describes the time domain behaviour of each mode:

$$T(r,z,t) = \sum_{n=0}^{\infty}\sum_{m=0}^{\infty} A(\beta_m,\eta_n)\underbrace{J_0(\beta_m r)sin(\eta_n z)}_{\text{spatial}}\underbrace{\mathcal{T}_{mn}(t)}_{temporal} \quad (6)$$

where $A(\beta_m,\eta_n)$ depends on the correlation between $g_v(r,z)$ and $J_0(\beta_m r)sin(\eta_n z)$ and

$$\mathcal{T}_{mn}(t) = \int_{t'=0}^{t} g_t(t')e^{-\alpha\lambda_{mn}^2(t-t')}dt' \quad (7)$$

i.e. the convolution of $g_t(t)$ and $e^{-\alpha\lambda_{mn}^2 t}$. $g_v(r,z)$ is the product of the optical absorption coefficient and the optical fluence, as defined in Eq. S2. By utilizing Eq. 6, we can generate spatial temperature distributions within the absorber and matrix at various

time points (Fig. 2b). In frequency domain $\mathcal{T}$ is the product of the Fourier transforms of $g_t(t)$ and $e^{-\alpha\lambda_{mn}^2 t}$, allowing an easy way to study location dependent amplitudes of temperature changes (see Fig. 2c)

Once $T(r,z,t)$ is known, following Noda et al.,[30] the vertical sample displacement u_z at the surface can be determined from Navier's equations for axisymmetric thermoelastic problems in cylindrical coordinates as (see Supplementary section S2):

$$u_z(r,h_{mat},t)=\sum_{n=0}^{\infty}\sum_{m=0}^{\infty}\frac{2(v-1)A(\beta_m,\eta_n)K}{\beta_m}\left(\frac{\eta_n^2}{\beta_m^2+\eta_n^2}+1\right)\underbrace{J_0(\beta_m r)}_{\text{spatial}}\underbrace{\mathcal{T}_{mn}(t)}_{\text{temporal}} \tag{8}$$

where K is the Restraint coefficient (see equation S39) and

$$A(\beta_m,\eta_n)=\frac{4}{\kappa h_{mat}R_{mat}^2}\frac{\iint_V r' J_0(\beta_m r')sin(\eta_n z')g(r',z')dr'dz'}{J_1^2(\beta_m R_{mat})\lambda_{nm}^2} \tag{9}$$

for a sphere, it is:

$$A(\beta_m,\eta_n)=\frac{8R_{abs}g_V}{\kappa h_{mat}R_{mat}^2}\frac{J_1(\beta_m R_{abs})sin(\eta_n z_0)sin(\eta_n R_{abs})}{J_1^2(\beta_m R_{mat})\lambda_{nm}^2\beta_m\eta_n} \tag{10}$$

Again, time domain and spatial domain behavior separated in (8).

Where R_{abs} is the radius of the absorber. Eq. 8 provides us with ability to represent the surface displacement either in the time domain or the frequency domain. This is illustrated in Fig. 2d as an example.

Comparison PSF model and FEM

To verify that the assumptions taken for the PSF model did not affect its ability to describe an actual AFM-IR experiment, the integrated temperature and surface displacement profiles calculated by the model were compared with those calculated using a FEM model of a spherical absorber consisting of PMMA embedded into a PE matrix placed on a silicon substrate. The displacement profiles conformed well to reality: spherical absorber and matrix were assigned literature values for thermal and

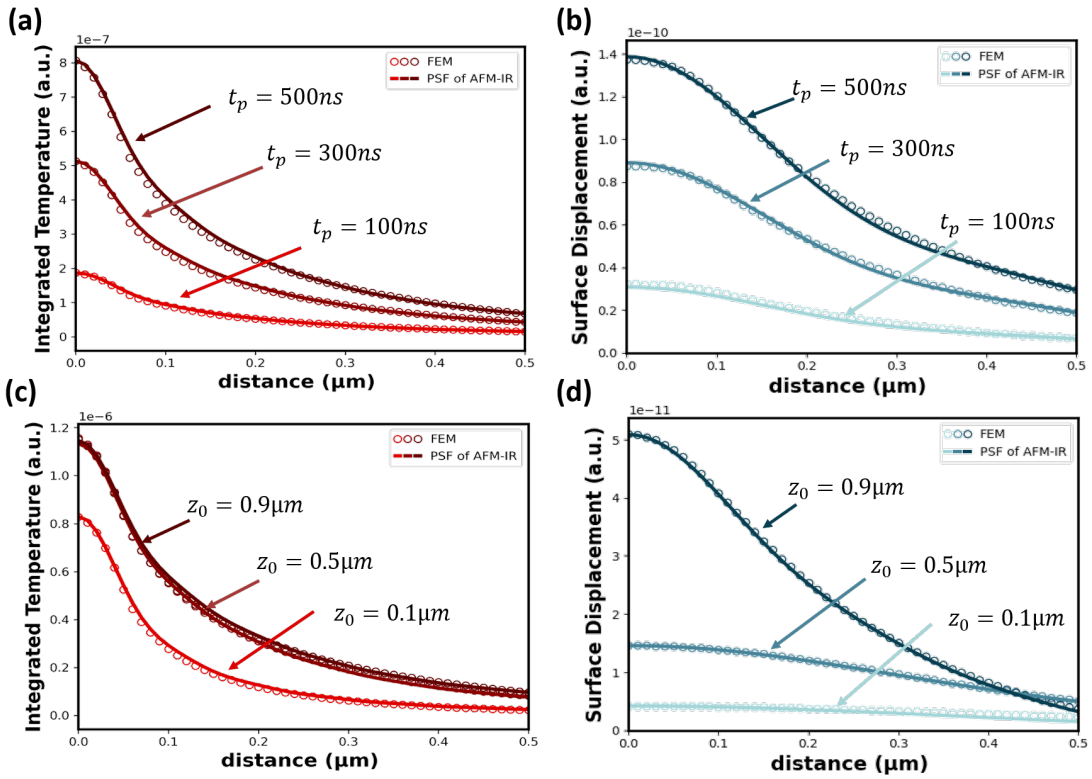

Figure 3: **Integrated temperature and displacement profile for three different laser pulse widths and depth positions of the absorber.** **(a)** Temperature profile and **(b)** thermo-elastic displacement profile are examined for three different pulse widths at a laser repetition rate of 500 kHz. The absorber is positioned at a depth of $z_0 = 0.9\,\mu m$. **(c)** Temperature profile and **(d)** thermo-elastic displacement profile are examined for three different depth positions of the absorber. At a laser repetition rate of 500 kHz and a pulse width of 100 ns.

mechanical properties of PMMA and PE, respectively. The substrate was not set to be a perfect heat sink but a Si layer (5 µm) and instead of an insulating boundary at the cover layer, here heat transduction through thermal diffusion in air (5 µm) was modeled. The material properties for simulations are listed in Supplementary Table 1. Unless stated otherwise, the following parameters remain constant in simulations involving the FEM and PSF models of AFM-IR: $R_{abs} = 70\,nm$, matrix thickness $h_{mat} = 1\,\mu m$, the matrix radius is $R_{mat} = 5\,\mu m$ (see Figure 2a for a sketch of the sample geometry).

Both models yield virtually identical integrated temperatures for all tested pulse widths (see Fig. 3a for the variation of integrated temperature at pulse widths of 100 ns, 300 ns and 500 ns). Both models also agree well when it comes to the dependence of

surface displacement on pulse width (Fig. 3b).

Both integrated temperature and surface displacement increase with increasing pulse width. However, it is evident that the surface displacement profile is much broader than the temperature profile. These results confirm that the thermo-elastic displacement has a nonlinear relationship with the temperature variation due to the presence of an inhomogeneous distribution of the heat source, which induces non-uniform strains in adjacent materials.

Furthermore, both models reveal distinct dependencies of integrated temperature and surface displacement on the absorber position (see Fig. 3c,d). Evidently, when the absorber is positioned closer to the surface, the surface displacement exhibits higher amplitude and a narrower profile, while the shape of the integrated temperature profile mainly depends on how quickly the heat can diffuse away from the absorber (i.e. it is narrower closer to the substrate). Likewise, a comparable dependency is evident in the surface temperature profiles (see Fig. S1).

Despite the PSF model of AFM-IR being designed for scenarios where the absorber is fully beneath the surface, we used the FEM model to understand how an absorber that extends partially beyond the surface would behave in AFM-IR. Surprisingly, we observed minimal difference in the displacement profile and amplitude for a bead that is just below the surface and one that is half below and half above the surface, as depicted in Fig. S2. In general there is a high level of agreement between the PSF model of AFM-IR and the FEM simulations, with a mean percentage difference between both models for integrated temperature and displacement data below 3% for all tested pulse widths and depth positions of the absorber (see Fig. S3), meaning that the simplifications of the PSF model do not noticeably affect its accuracy.

The same agreement was found when other experimental parameters were adjusted, such as sample size R_{abs}, specific heat capacity C_p and thermal conductivity κ (see Fig. S4). These results indicate that the surface displacement magnitude is roughly in proportion to the absorber's volume (Fig. S4a), while the full width at half maximum (FWHM) of the displacement profile does not show a proportional increase with the

absorber's size (see Fig. S4b). Moreover, the physical properties of the matrix material play a crucial role in the signal intensity and and the spatial resolution (given by the shape of the surface displacement). A matrix material with low heat capacity and thermal conductivity leads to higher signal intensity at the surface (Fig. S4c, e). This occurs due to the rapid heating characteristic of a material with low specific heat capacity, coupled with its limited thermal conductivity that impedes efficient heat conduction. Consequently, heat is redistributed from the absorber into the matrix material more slowly, resulting in a higher temperature and corresponding higher thermal expansion. On the other hand, a matrix material with high specific heat capacity and low thermal conductivity shows narrower surface displacement profiles. The increased heat capacity facilitates superior thermal confinement, reducing the spread of heat and enhancing the spatial resolution of the imaging (Fig. S4d). Additionally, the low thermal conductivity helps to minimize heat dissipation, further enhancing the resolution of AFM-IR imaging (Fig. S4f).

Comparison of model and experiment

A sample resembling the simulated structure using FEM and PSF model was prepared using PMMA beads with diameters of approximately 140 nm. These beads were suspended in a PE matrix and subsequently microtomed into thin slices with a thickness of 1 µm (refer to the Methods section for more details). The buried absorber (see Fig. 4a) was detected using the 1730 cm^{-1} carbonyl band of PMMA (see Fig. 4b) which can be clearly distinguished from the matrix spectrum. The AFM-IR absorption image (also referred to as "chemical image") at 1730 cm^{-1} shows a single PMMA bead (see Fig. 4c) with a FWHM determined from the cross section through the chemical image of 121 nm.

Here, we find another utility of the FEM based model, namely that it also allows us model the heat flow across the interface between PMMA and PE, such as interfacial roughness, compositional disorder or general interfacial thermal resistance[33,34] which could affect the thermal diffusion and thus the AFM-IR signal. To address

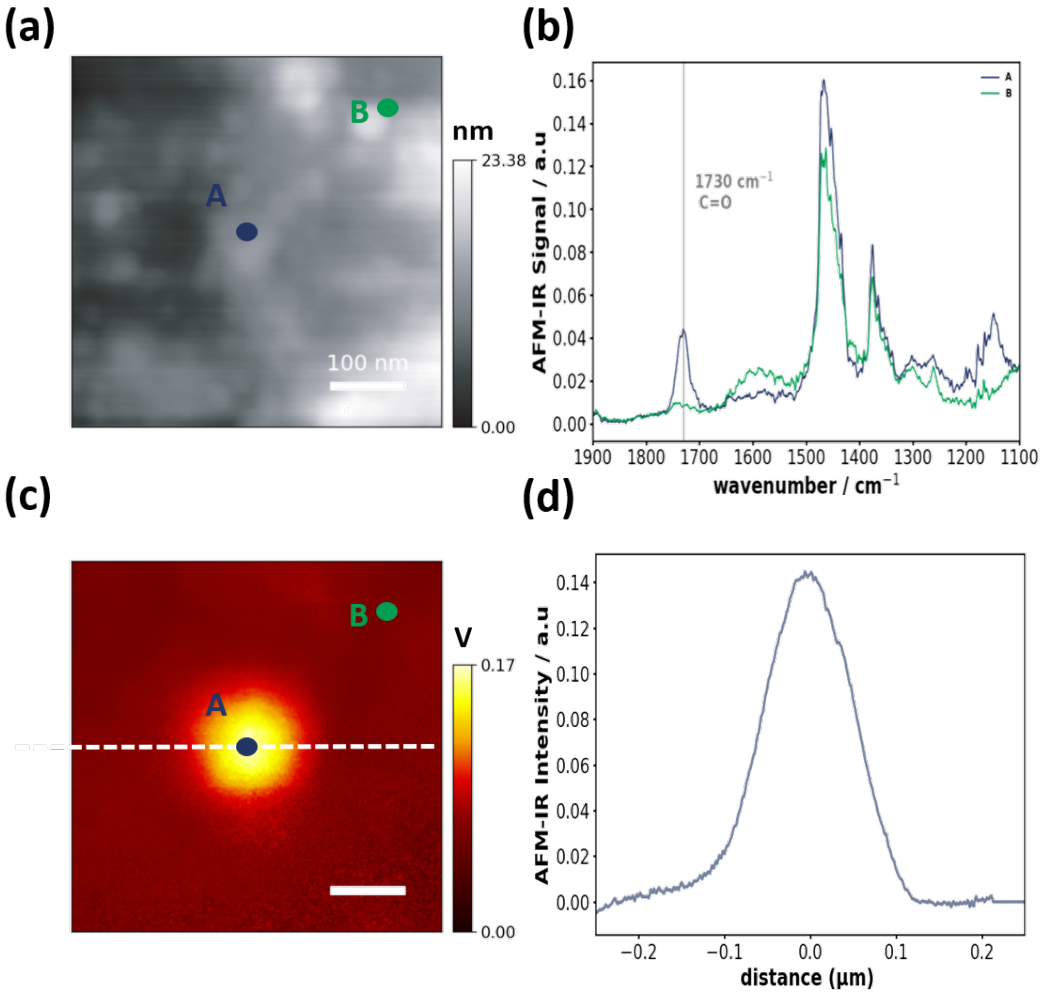

Figure 4: **PMMA beam measurement with laser repetition rate** 508 kHz**, pulse width** 200 ns. **(a)** AFM topography image of a PMMA nanoparticle. **(b)** AFM-IR spectra obtained on the position A and B, respectively. **(c)** Corresponding AFM-IR chemical map at 1730 cm^{-1}. The dashed line corresponds to the profile in (d). **(d)** Cross section profile of the AFM-IR signal distribution.

these potential effects, we incorporated interfacial thermal resistance ($R_{PMMA/PE}$) between PMMA and PE into the finite element simulations. However, to the best of our knowledge, no literature values exist for the interfacical thermal resistance between $R_{PMMA/PE}$ and interfacial thermal resistance values are generally associated with high uncertainties[35,36]. We found the best match between experimental data and model to lie around 2.2 m^2K/MW, with higher (2.5 m^2K/MW) and lower (2.0 m^2K/MW) $R_{PMMA/PE}$ leading to results that still lie inside the error bars of the measurement

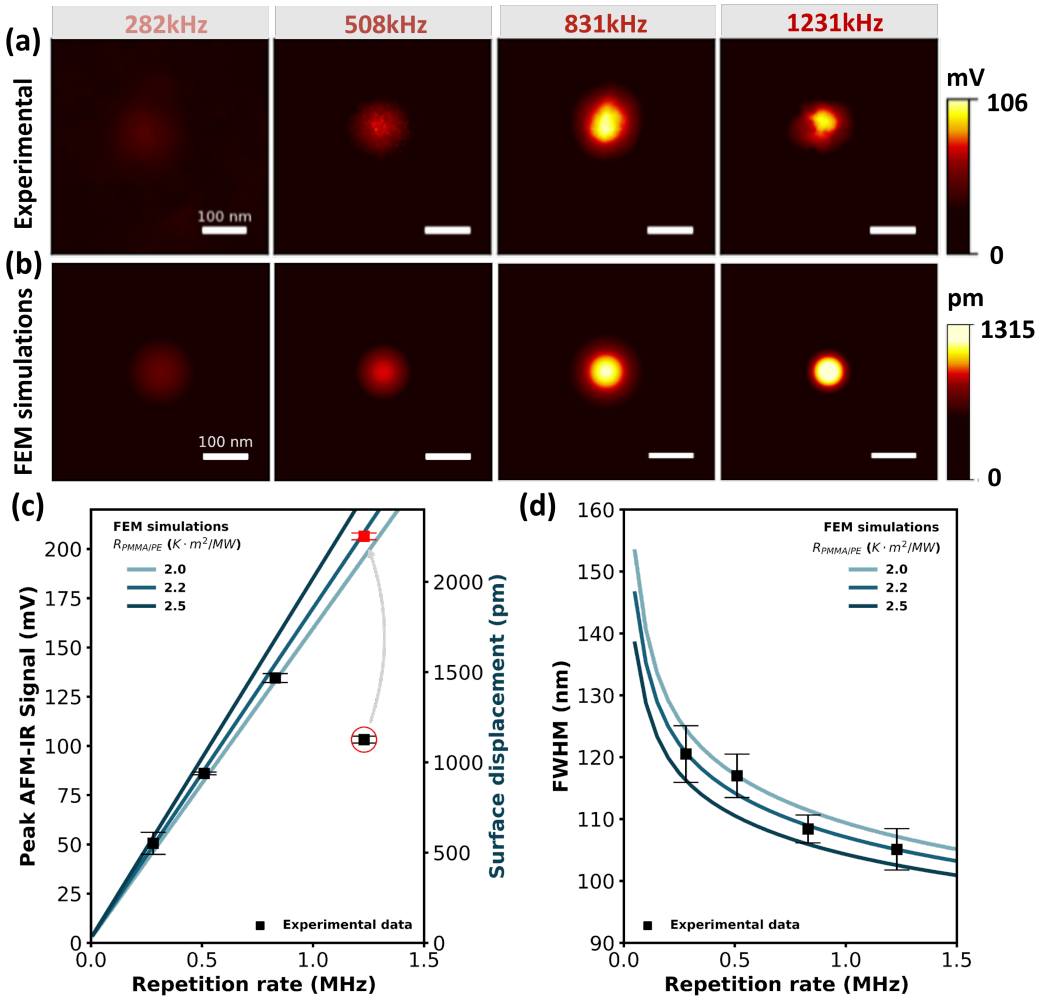

Figure 5: **AFM-IR images were obtained for various laser repetition rates.** **(a)** Experimental AFM-IR images were obtained using a series of laser repetition rates at a pulse width of 100 ns. **(b)** Simulated AFM-IR images under the same experimental parameters. Considering a peak laser power of 4.5 mW, beam diameter r_{laser} = 10 µm, diameter of 140 nm for the absorber, positioned at a depth of 0.93 µm, tightly under the surface. **(c)** Peak amplitudes of AFM-IR signal in dependence on laser repetition rates. The simulated line represents the trend of the peak surface displacement based on FEM simulations. The data point circled was measured at half the expected signal amplitude (see main text for explanation) **(d)** FWHM of AFM-IR signal cross section was measured at laser repetition rates of 282 kHz, 508 kHz, 831 kHz, and 1231 kHz. The reported measurements include the mean value as well as the maximum deviation from repeated measurements. The FEM simulated line represents the trend of the FWHM as a function of laser repetition rates. The simulation presented in Fig. S7 is based on the PSF model and does not include consideration for the thermal resistance at the interface.

(see Fig. 5d). These values are comparable to those used by others to simulate AFM-IR experiments.[9]

The model and experiment both show a decrease in FWHM of the AFM-IR signal with increasing repetition rate (see Fig. 5a,b,d).

They also show the same increase for peak amplitude at constant pulse width and increasing repetition rate (see Fig. 5c). The increasing peak amplitude can be attributed to the increasing duty cycle and thus increasing energy deposited in the absorber. The peak amplitude at the highest tested frequency (1231 kHz) deviates from the trend seen for the other frequency but follows the FWHM trend (see Fig. 5c,d). This is due to the fact that at this setting a duty cycle of 12.3 % had been reached which goes beyond the specifications of the laser used. In this regime the EC-QCLs control circuit will skip every other pulse so as to stay within the maximum duty cycle specifications of the device and avoid damage, leading to a 50 % reduction in peak amplitude. The FWHM is not affected by this.

We use the FWHM of the AFM-IR signal distribution profile, as depicted in Fig. 5d to determine the achievable spatial resolution. Experiments and models agree that increasing the laser repetition rates led to a decrease in FWHM, indicating improved spatial resolution. In the following section, we show that this effect can be understood through the PSF model.

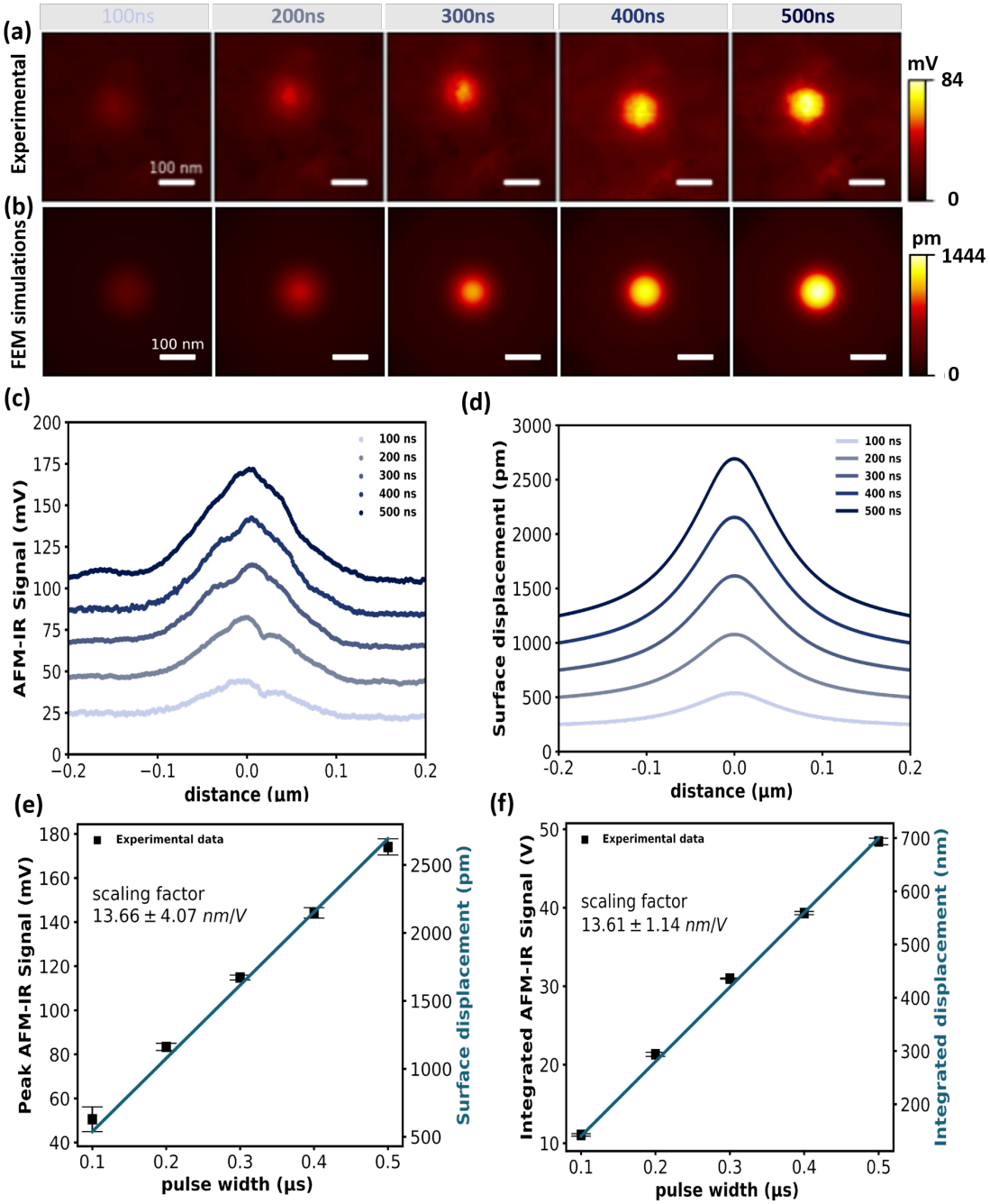

Figure 6: **AFM-IR signal dependence on pulse width.** **(a)** Experimental AFM-IR images were obtained using a series of laser pulse widths ranging from 100 ns to 500 ns at a laser repetition rate of 282 kHz. To highlight the distinct contrast between the figures acquired at different frequencies, all images were subtracted by their respective minimum values. The figures displaying the original minimum values are presented in Fig. S8. **(b)** Simulated AFM-IR images under the same experimental parameters. Considering laser power 4.5 mW, a diameter of 100 nm for the absorber, positioned at a depth of 0.93 µm. **(c)** The experimental AFM-IR signal profile over axial displacement measured at different pulse widths. **(d)** FEM simulation of surface displacement profiles at different pulse widths. **(e)** Peak AFM-IR signal and simulated peak surface displacement in dependence on pulse widths. The reported measurements represent the mean values with the maximum deviation from repeated measurements. **(f)** Integrated AFM-IR signal and simulated integrated surface displacement in dependence on pulse widths.

The model and simulation also agree well when it comes to the effect of pulse width. When keeping the repetition rate around 282 kHz and varying the pulse width from 100 ns to 500 ns at constant peak pulse power, a linear dependence of peak and integrated amplitude on the pulse width is found (see Figs.6). To compare modeled and measured amplitude a scaling factor is required, as the models directly output surface deflection, while the AFM-IR signal is proportional to surface deflection but has several sensitivity constants that are difficult to determine.[17] We use a scaling factor of $(13.61 \pm 1.14)\,\mathrm{nm/V}$, which was determined as described in **Methods**.

This effect, too, is due to the increasing duty cycle and thus increasing energy deposited in the absorber. This effect is not true for arbitrary long pulse widths, as will be discussed below.

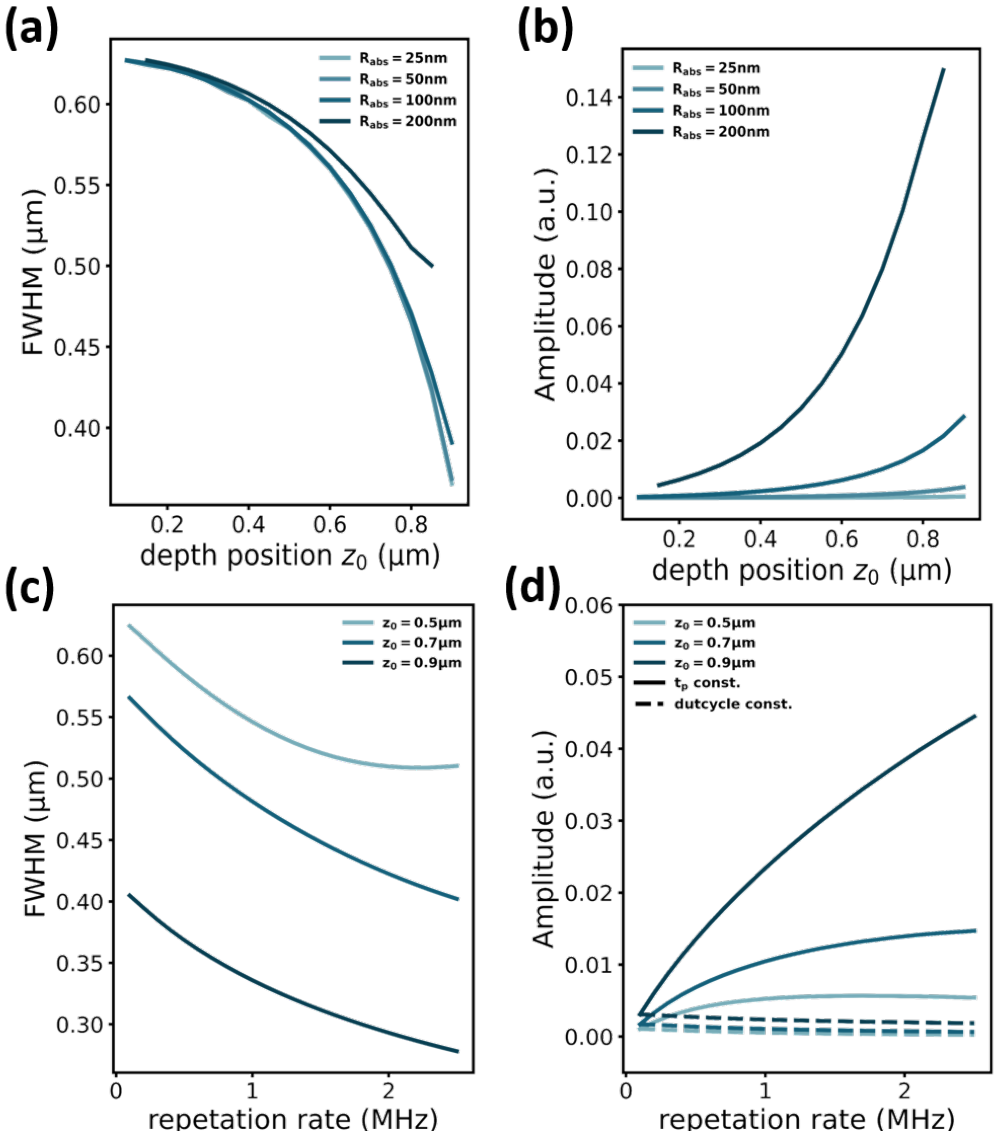

Figure 7: **FWHM and amplitude exhibit dependencies on the position of absorber depths and laser repetition rates.** **(a)** FWHM and **(b)** amplitude are examined at various absorber depth positions for four different absorber sizes. The laser pulse has a duration of 100 ns, and the repetition rate is 500 kHz. **(c)** FWHM and **(d)** amplitude are examined at different laser repetition rates for three distinct absorber depth positions. Solid lines represent simulations at a constant laser pulse duration of 100 ns, and dash lines represent simulations with a constant duty cycle of 1%. The absorber has a radius of 50 nm.

Effects of experimental parameters on the AFM-IR signal

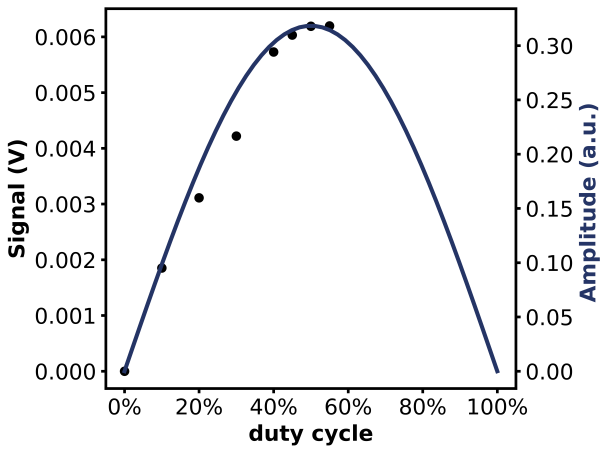

Figure 8: The measured laser power and calculated signal amplitude as a function of duty cycle.

Having established that the PSF and FEM model and FEM model and experiment, respectively, agree well, we can now leverage the PSF model to understand the effects of experimental parameters on the AFM-IR signal.

As the PSF model can describe the signal of a three dimensional absorber, in addition to time/frequency domain behaviour[9] it can also describe the lateral extension of the deflection caused by an absorber, which allows to determine the spatial resolution of the AFM-IR measurement. In general, modes with higher β_m will lead to a narrower profile due to the only r dependent term $J_0(\beta_m r)$ in (8). These narrower modes will have a faster decay in time as λ_{mn} increases with m affecting the time dependent term $\mathcal{T}_{mn}(t)$ defined in (7).

Thus, resonance enhanced AFM-IR at higher frequencies and other AFM-IR techniques that use high frequencies by default, such as tapping mode AFM-IR and surface sensitive AFM-IR provide a better lateral spatial resolution.

The PSF model also shows a relationship between the FWHM of the surface deflection and the distance $h_{mat} - z_0$ of the absorber from the surface. The further the absorber is from the surface the wider the FWHM (see Fig. 7a). This behaviour can be explained by looking at the z_0 dependence of $A(\beta_m, \eta_n)$. For a spherical absorber this

can be easiest explained through the following part of $A(\beta_m, \eta_n) \sin(\eta_n z_0) \sin(\eta_n R_{abs})$ (see equation 10). This expression will always be positive for low z_0 but for $z_0 \approx h_{mat}$ will be positive for even n be positive and for odd n be negative. As the mode shape in $r \propto J_0(\beta_m r)$ this means that for absorbers close to the surface the wider lower order modes in m for $n = 0$ are counteracted by negative contributions from $n > 0$.

The $\sin(\eta_n z_0) \sin(\eta_n R_{abs})$ term also explains the higher surface deflection for absorbers close to the surface: at $z_0 \propto 0$, $\sin(\eta_n z_0)$ will also be close to zero.

Taking a closer look at the frequency dependence of the spatial resolution, (7) allows us to understand the effect of pulse width on the achievable spatial resolution. For a rectangular pulse $\prod\left(\frac{t}{t_p}\right)$ (e.g. in the case of an EC-QCL), in the frequency domain

$$\mathcal{T}_{mn}(f) = \frac{2\alpha\lambda_{mn}^2}{\alpha^2\lambda_{mn}^4 + 4\pi f^2} \cdot t_p \operatorname{sinc}(t_p f) \tag{11}$$

Thus, when the laser is pulsed at a fixed frequency the Fourier transformed $\prod$ merely acts as a scaling factor that affects all $A(\beta_m, \eta_n)$ in the same way. Pulse width thus only affects the signal amplitude but not the spatial resolution. We can also see that the pulse width does affect overall signal amplitude. It reaches a maximum at $t_p = \frac{1}{2f}$ and then decreases back down to 0 at $t_p = \frac{1}{f}$. Note that f here is not necessarily the laser repetition rate f_{rep} but the frequency at which the signal is demodulated. Hence, when demodulating the AFM-IR signal at a multiple of the laser repetition rate (as is sometimes done to reach cantilever resonances beyond the maximum pulse repetition rate of the laser) care has to be taken, that the product of the demodulation frequency and pulse width $f t_p \leq 0.5$ (see the relationship between laser amplitude and duty cycle in Fig. 8). Increasing $f t_p > 0.5$ does not increase the amplitude of the signal and only leads to unnecessary sample heating. (An illustration of the relationship between pulse width, amplitude and frequency can be found in Fig. S5).

As mentioned above, increasing the pulse repetition rate will narrow the FWHM of the surface deflection (i.e. improve spatial resolution). However, this does not affect absorbers at all depths in the same way (see Fig. 7c). Here, for absorbers buried

deeper below the surface a "levelling out" effect can be seen, whereby further increase of the repetition rate does not improve the spatial resolution.

Finally, the PSF model also helps to explain the depth resolution of the surface sensitive AFM-IR (see Fig. 7d). At constant pulse width the peak amplitude caused by an absorber buried deeper inside the sample plateaus at lower frequencies than that of those closer to the surface. When the experiment is conducted at constant duty cycle, this appears as an overall decrease of the peak amplitude of the buried absorber compared to that of absorbers closer to the surface.

Conclusions

This work establishes an analytical expression that describes, for the first time, the surface deflection caused by a three dimensional absorber in an AFM-IR experiment. This point spread function model provides a detailed understanding of the photothermal expansion and AFM-IR signal generation processes. Based on this model we can understand the effect of experimental parameters and sample geometry on signal amplitude and spatial resolution.

The PSF model was rigorously validated through comparisons with finite element method (FEM) simulations and experimental data.

The developed PSF model explains that increasing the pulse width enhanced the signal as long as the product of pulse width and demodulation frequency is kept below 0.5. Furthermore, while some researchers[9] have theorized that longer pulse width might degrade spatial resolution we did not see this effect in our experimental data. Here, too, our experimental data agree with the PSF model, which also does not find a direct relation between pulse width and spatial resolution.

The demodulation frequency is found to be the main factor under control of the AFM-IR user for a given sample and cantilever that affects spatial resolution. Higher frequency improves resolution. At constant pulse width it also increases peak amplitude.

The PSF model can also be used to study vertical resolution of high frequency AFM-IR modes, showing that the peak signal amplitude from absorber far from the surface will decay with increasing demodulation frequency.

In comparing experimental data and FEM model we have identified the interfacial thermal resistance between phases as a significant contribution to the AFM-IR signal. While the determination of interfacial thermal resistance in AFM-IR using custom transducers has previously been demonstrated[7,37] specialized, high frequency AFM-IR tips were demonstrated for the determination of this often elusive parameter, our results hint at alternative approach that leverages the frequency dependent AFM-IR image combined with modeling. In this work, the interfacial thermal resistance between PMMA absorber and PE was found to be $\approx 2.2\,\mathrm{m^2K/MW}$.

The combination of optical and photo-elastic effects in AFM-IR also need to be taken into account when evaluating spectra, as peak amplitude caused by an absorber not only depend on its vertical but also its lateral extension.

While our model does not take into account acoustic waves, Chae et al. reported the detection of such waves in the air in an AFM-IR experiment using a nanophotonic transducer[7], and Raschke et al. studied them in the context of photoinduced force experiments[38]. Despite regarding the acoustic wave as negligible in our current study, investigating the coupling of photothermal and photoacoustic effects would constitute a valuable addition and could potentially contribute to a better understanding of how to either use these phenomena to gain additional insight into the sample or better understand how to remove their contribution to the AFM-IR signal.

The developed PSF model of AFM-IR provides researchers with a powerful tool for quantitative analysis and optimization of nanoscale chemical imaging experiments. Beyond the applications and results shown in this work a conversion to Cartesian coordinates can be envisioned. This would allow to study more complex samples. As the PSF model is significantly more efficient than a comparable FEM approach it can provide deeper insights into advanced, non-linear AFM-IR techniques, such as surface sensitive AFM-IR. Potentially, the model could also be used to combine

AFM-IR images taken at different frequencies to perform tomography to determine the vertical makeup of a sample.

Methods

Sample Preparation

The PE/PMMA sample was prepared by melting and mixing a polyethylene (PE) matrix (average Mw 35.000, Sigma Aldrich) just above the melting temperature (Tm = 116 °C) while keeping in motion through, vigorous stirring and subsequently adding nano-beads of Poly(methyl methacrylate) (PMMA, Tm = 160 °C) with average diameter 140 nm (PolyAn Pink, PolyAn GmbH). The beads are dispersed in a water solution with a solid content of 1 % and were pipetted onto the molten PE. This evaporates the water but does not melt PMMA. Stirring was continued until beads were thoroughly mixed into the PE. Then the mixture was cooled to room temperature. For further drying, the sample was placed into an oven (105 °C) for 3 hours.

The sample was ultra-cryomicrotomed to a thickness of 1 µm and placed on Si substrates for measurements.

AFM-IR experimental and data collection

All AFM-IR data were collected using a nanoIR3s (Bruker) controlled by Analysis Studio (Anasys Instruments, v3.15).

Experiments were conducted using an overall gold coated contact mode cantilever (Cont-GB-C, BudgetSensors Innovative Solutions Bulgaria Ltd.) with a nominal first resonance frequency of (13 ± 4) kHz and a nominal spring constant between $0.04\,\mathrm{N\,m^{-1}}$ and $0.40\,\mathrm{N\,m^{-1}}$. As source for photothermal excitation a mid-IR external cavity quantum cascade laser (EC-QCL) (MIRcat-QT, DRS Daylight Solutions Inc.) was used. All AFM-IR measurements were performed in resonance enhanced contact mode AFM-IR. For AFM-IR images a 500 nm × 500 nm area was scanned with a line rate of 0.1 Hz (lateral speed $100\,\mathrm{nm\,s^{-1}}$) and a resolution of 400 pixels per line at 200 lines. For chemical imaging the distinct carbonyl-stretching band of PMMA (C=O) at $1730\,\mathrm{cm^{-1}}$ was

selected and pulse peak power was set as 15 mW. The polarization of the laser source is set to 0 degrees in respect to the sample plane. The laser repetition rate was kept at the frequency of the contact resonance of the cantilever using a phase-locked loop (PLL).

The experiments were performed at a series of laser pulse widths of 100 ns, 200 ns, 300 ns, 400 ns, 500 ns each at laser repetition rates of 282 kHz, 508 kHz, 831 kHz, and 1231 kHz. For each laser – pulse width and repetition rate setting three IR images were collected. Simultaneously with the IR images (trace and retrace), also height images (trace and retrace), deflection channel (trace and retrace) and the PLL frequency channel (trace and retrace) were recorded.

The AFM-IR instrument and laser beam paths were encased and purged with dry air.

Scaling factor determination

The original figures of Fig. 5 and 6 with the their respective minimum values are presented in Fig. S6 and S8. Fig. 5c and d illustrate the cross section through the chemical images and FEM simulations at different pulse widths from Fig. 5a and b. In the absence of consideration for the interfacial thermal resistance between PMMA beads and PE, the simulated surface displacement profiles exhibit much greater width compared to the cross-section profiles observed in the experiments, as depicted in Fig. S9. distribution of the experimental results among the three simulated lines, emphasizing the impact of PMMA/PE on the simulation outcomes.

Fig. 6e and f depict that the simulated peak and integrated surface displacement exhibit a linear growth trend with the pulse width. When compared with the experimental results, scaling factors (accounting for a range of experimental sensitivity factors) of 13.66 ± 4.07 nm/V and 13.61 ± 1.14 nm/V were obtained for the surface displacement and the AFM-IR signal, respectively. Calculated scaling factors for the surface displacement and the AFM-IR signal at each pulse width are shown on Fig. S10.

Laser power duty cycle measurement

A custom EC-ICL (ALPES Lasers SA) was used to probe the behavior of the AFM-IR signal at high duty cycle (see Fig.8). The device emits between 2800 cm^{-1} to 3100 cm^{-1} and achieves pulse lengths of up to 3000 ns at repetition rates up to 180 kHz at >10 mW peak power and up to 100% duty cycle.

Author information

Corresponding Author

*georg.ramer@tuwien.ac.at

ORCID

Yide Zhang: 0000-0002-2675-739X

Ufuk Yilmaz: 0009-0009-3572-5267

Liam O'Faolain: 0000-0003-1160-7441

Bernhard Lendl: 0000-0003-3838-5842

Georg Ramer: 0000-0001-8307-5435

Author Contributions

Y.Z. and U.Y. prepared samples, performed experiments and drafted the manuscript. Y.Z. performed FEM simulations and developed the PSF model with input from G.R.. G.R. supervised U.Y. and Y.Z. in all experiments and evaluations. G.R., L.O'F. and B.L. conceptualized the study and proposed the project. B.L. and L.O'F. acquired the funding. All have read and revised the manuscript.

Acknowledgement

This work was funded with financial support from the European Union's Horizon 2020 research and innovation programme. The authors Y.Z., L.O'F., G.R., and B.L. acknowledge the Marie Skłodowska-Curie project "OPTAPHI" under grant agreement

No. 860808. U.Y., and G.R. acknowledge the Europen Commissions's Horizon 2020 project "PeroCUBE" under grant agreement No. 861985. G.R. also acknowledges support from Europen Commissions's Horizon 2020 project "TUMOR-LN-oC" under grant agreement number 953234. The authors would like to thank Gustavo Vinicius Bassi Lukasievicz and Andrew Cashman for their valuable input and the discussions. Furthermore, the authors would also like to thank Jakob Gruber and Karin Whitmore for microtoming some samples using facilities at the University Service Centre for Transmission Electron Microscopy (USTEM), TU Wien.

Supporting Information Available

A PDF file including of additional figures S1 to S12, table S1 and the additional derivations for equations in the main text is available free of charge.

Code and raw data to generate all figures is available on Zenodo: `https://dx.doi.org/10.5281/zenodo.10518024`

Declarations

The authors declare that they have no known competing financial interests or personal relationships that could have appeared to influence the work reported in this paper.

References

1. Centrone, A. Infrared Imaging and Spectroscopy Beyond the Diffraction Limit. *Annual Review of Analytical Chemistry* **2015**, *8*, 101–126.

2. Dazzi, A.; Prater, C. B. AFM-IR: Technology and Applications in Nanoscale Infrared Spectroscopy and Chemical Imaging. *Chemical Reviews* **2017**, *117*, 5146–5173.

3. Katzenmeyer, A. M.; Holland, G.; Chae, J.; Band, A.; Kjoller, K.; Centrone, A. Mid-infrared spectroscopy beyond the diffraction limit via direct measurement of the photothermal effect. *Nanoscale* **2015**, *7*, 17637–17641.

4. Dazzi, A.; Prater, C. B.; Hu, Q.; Chase, D. B.; Rabolt, J. F.; Marcott, C. AFM–IR: Combining Atomic Force Microscopy and Infrared Spectroscopy for Nanoscale Chemical Characterization. *Applied Spectroscopy* **2012**, *66*, 1365–1384.

5. dos Santos, A. C. V.; Lendl, B.; Ramer, G. Systematic analysis and nanoscale chemical imaging of polymers using photothermal-induced resonance (AFM-IR) infrared spectroscopy. *Polymer Testing* **2022**, *106*, 107443.

6. Ruggeri, F. S.; Mannini, B.; Schmid, R.; Vendruscolo, M.; Knowles, T. P. J. Single molecule secondary structure determination of proteins through infrared absorption nanospectroscopy. *Nature Communications* **2020**, *11*, 2945.

7. Chae, J.; An, S.; Ramer, G.; Stavila, V.; Holland, G.; Yoon, Y.; Talin, A. A.; Allendorf, M.; Aksyuk, V. A.; Centrone, A. Nanophotonic Atomic Force Microscope Transducers Enable Chemical Composition and Thermal Conductivity Measurements at the Nanoscale. *Nano Letters* **2017**, *17*, 5587–5594.

8. Ramer, G.; Aksyuk, V. A.; Centrone, A. Quantitative chemical analysis at the nanoscale using the PTIR technique. *Analytical Chemistry* **2017**, *89*, 13524–13531.

9. J. Schwartz, J.; S. Jakob, D.; Centrone, A. A guide to nanoscale IR spectroscopy: resonance enhanced transduction in contact and tapping mode AFM-IR. *Chemical Society Reviews* **2022**, *51*, 5248–5267, Publisher: Royal Society of Chemistry.

10. Lu, F.; Jin, M.; Belkin, M. A. Tip-enhanced infrared nanospectroscopy via molecular expansion force detection. *Nature Photonics* **2014**, *8*, 307–312.

11. V. D. dos Santos, A. C.; Tranchida, D.; Lendl, B.; Ramer, G. Nanoscale chemical characterization of a post-consumer recycled polyolefin blend using tapping mode AFM-IR. *The Analyst* **2022**, *147*, 3741–3747.

12. Tang, F.; Bao, P.; Su, Z. Analysis of Nanodomain Composition in High-Impact Polypropylene by Atomic Force Microscopy-Infrared. *Analytical Chemistry* **2016**, *88*, 4926–4930.

13. Baldassarre, L.; Giliberti, V.; Rosa, A.; Ortolani, M.; Bonamore, A.; Baiocco, P.; Kjoller, K.; Calvani, P.; Nucara, A. Mapping the amide I absorption in single bacteria and mammalian cells with resonant infrared nanospectroscopy. *Nanotechnology* **2016**, *27*, 075101.

14. Dazzi, A.; Prazeres, R.; Glotin, F.; Ortega, J.; Al-Sawaftah, M.; de Frutos, M. Chemical mapping of the distribution of viruses into infected bacteria with a photothermal method. *Ultramicroscopy* **2008**, *108*, 635–641.

15. Yuan, Y.; Chae, J.; Shao, Y.; Wang, Q.; Xiao, Z.; Centrone, A.; Huang, J. Photovoltaic Switching Mechanism in Lateral Structure Hybrid Perovskite Solar Cells. *Advanced Energy Materials* **2015**, *5*, 1500615.

16. Houel, J.; Sauvage, S.; Boucaud, P.; Dazzi, A.; Prazeres, R.; Glotin, F.; Ortéga, J.-M.; Miard, A.; Lemaître, A. Ultraweak-Absorption Microscopy of a Single Semiconductor Quantum Dot in the Midinfrared Range. *Physical Review Letters* **2007**, *99*, 217404.

17. Dazzi, A.; Glotin, F.; Carminati, R. Theory of infrared nanospectroscopy by photothermal induced resonance. *Journal of Applied Physics* **2010**, *107*, 124519.

18. Dazzi, A. In *Thermal Nanosystems and Nanomaterials*; Volz, S., Ed.; Springer Berlin Heidelberg: Berlin, Heidelberg, 2009; Vol. 118; pp 469–503, Series Title: Topics in Applied Physics.

19. Morozovska, A. N.; Eliseev, E. A.; Borodinov, N.; Ovchinnikova, O. S.; Morozovsky, N. V.; Kalinin, S. V. Photothermoelastic contrast in nanoscale infrared spectroscopy. *Applied Physics Letters* **2018**, *112*, 033105.

20. Schwartz, J. J.; Pavlidis, G.; Centrone, A. Understanding Cantilever Transduction Efficiency and Spatial Resolution in Nanoscale Infrared Microscopy. *Analytical Chemistry* **2022**, *94*, 13126–13135.

21. Lahiri, B.; Holland, G.; Centrone, A. Chemical Imaging Beyond the Diffraction Limit: Experimental Validation of the PTIR Technique. *Small* **2013**, *9*, 439–445.

22. Quaroni, L. Understanding and Controlling Spatial Resolution, Sensitivity, and Surface Selectivity in Resonant-Mode Photothermal-Induced Resonance Spectroscopy. *Analytical Chemistry* **2020**, *92*, 3544–3554.

23. V. D. dos Santos, A. C.; Heydenreich, R.; Derntl, C.; Mach-Aigner, A. R.; Mach, R. L.; Ramer, G.; Lendl, B. Nanoscale Infrared Spectroscopy and Chemometrics Enable Detection of Intracellular Protein Distribution. *Analytical Chemistry* **2020**, *92*, 15719–15725.

24. Ma, X.; Pavlidis, G.; Dillon, E.; Kjoller, K.; Berrie, B.; Centrone, A. Nanoscale IR spectroscopy: From Principles to Nanoscale Imaging and Identification of Metal Soaps. *Microscopy and Microanalysis* **2021**, *27*, 2814–2815.

25. Kenkel, S.; Gryka, M.; Chen, L.; Confer, M. P.; Rao, A.; Robinson, S.; Prasanth, K. V.; Bhargava, R. Chemical imaging of cellular ultrastructure by null-deflection infrared spectroscopic measurements. *Proceedings of the National Academy of Sciences* **2022**, *119*, e2210516119, Publisher: Proceedings of the National Academy of Sciences.

26. Bai, F.; Bertram, R.; Karamched, B. R. A closed-loop multi-scale model for intrinsic frequency-dependent regulation of axonal growth. *Mathematical Biosciences* **2022**, *344*, 108768.

27. Kenkel, S.; Mittal, S.; Bhargava, R. Closed-loop atomic force microscopy-infrared spectroscopic imaging for nanoscale molecular characterization. *Nature Communications* **2020**, *11*, 3225.

28. Mathurin, J.; Deniset-Besseau, A.; Dazzi, A. Advanced Infrared Nanospectroscopy Using Photothermal Induced Resonance Technique, AFMIR: New Approach Using Tapping Mode. *Acta Physica Polonica A* **2020**, *137*, 29–32.

29. Mathurin, J.; Deniset-Besseau, A.; Bazin, D.; Dartois, E.; Wagner, M.; Dazzi, A. Photothermal AFM-IR spectroscopy and imaging: Status, challenges, and trends. *Journal of Applied Physics* **2022**, *131*, 010901.

30. Noda, N.; Hetnarski, R. B.; Tanigawa, Y. *Thermal stresses*, 2nd ed.; Taylor & Francis: New York, 2003.

31. Balasubramanian, G.; Puri, I. K. Heat conduction across a solid-solid interface: Understanding nanoscale interfacial effects on thermal resistance. *Applied Physics Letters* **2011**, *99*, 013116.

32. Cole, K. D., Ed. *Heat conduction using Green's functions*, 2nd ed.; Series in Computational and Physical Processes in Mechanics and Thermal Sciences; CRC Press: Boca Raton, 2011.

33. Hopkins, P. E. Thermal Transport across Solid Interfaces with Nanoscale Imperfections: Effects of Roughness, Disorder, Dislocations, and Bonding on Thermal Boundary Conductance. *ISRN Mechanical Engineering* **2013**, *2013*, 1–19.

34. Song, J.; Zhang, Y. Effect of an interface layer on thermal conductivity of polymer composites studied by the design of double-layered and triple-layered composites. *International Journal of Heat and Mass Transfer* **2019**, *141*, 1049–1055.

35. Zheng, K.; Zhu, J.; Ma, Y.-M.; Tang, D.-W.; Wang, F.-S. Interfacial thermal resistance between high-density polyethylene (HDPE) and sapphire. *Chinese Physics B* **2014**, *23*, 107307.

36. Losego, M. D.; Moh, L.; Arpin, K. A.; Cahill, D. G.; Braun, P. V. Interfacial thermal conductance in spun-cast polymer films and polymer brushes. *Applied Physics Letters* **2010**, *97*, 011908.

37. Wang, M.; Ramer, G.; Perez-Morelo, D. J.; Pavlidis, G.; Schwartz, J. J.; Yu, L.; Ilic, R.; Aksyuk, V. A.; Centrone, A. High Throughput Nanoimaging of Thermal Conductivity and Interfacial Thermal Conductance. *Nano Letters* **2022**, *22*, 4325–4332.

38. O'Callahan, B. T.; Yan, J.; Menges, F.; Muller, E. A.; Raschke, M. B. Photoinduced Tip–Sample Forces for Chemical Nanoimaging and Spectroscopy. *Nano Letters* **2018**, *18*, 5499–5505.